Lattice dynamics and topological surface phonon states in cuprous oxide Cu_2O

Zhenwei Wang,[1] Weiqing Zhou,[1] A. N. Rudenko,[1,2,3,*] and Shengjun Yuan[1,†]

[1]*Key Laboratory of Artificial Micro- and Nano-structures of Ministry of Education and School of Physics and Technology, Wuhan University, Wuhan 430072, China*

[2]*Institute for Molecules and Materials, Radboud University, Heijendaalseweg 135, NL-6525 AJ Nijmegen, The Netherlands*

[3]*Department of Theoretical Physics and Applied Mathematics, Ural Federal University, 620002 Ekaterinburg, Russia*

(Received 16 November 2020; revised 18 January 2021; accepted 19 April 2021; published 17 May 2021)

The topological phonon state of quantum matter is an emerging field that has been attracting considerable interest. For instance, Weyl phonons in transition-metal monosilicides have been proposed theoretically and identified experimentally. However, topological phonon nodal net states are not well studied due to the lack of realistic materials. Here, based on first-principles calculations and effective model analysis, we propose an existing material—cuprous oxide—to host the nodal net phonons. The nontrivial phonon surface states and uncovered phononic arcs are clearly visible on k-resolved phonon spectra, which are amenable to experimental detection. Our findings offer a possible platform for realizing topologically nontrivial phonon states and their applications.

DOI: 10.1103/PhysRevB.103.195137

I. INTRODUCTION

Quasiparticle excitations in topological semimetals have attracted enormous interest in the fields of condensed-matter physics and material science [1–6]. It can be attributed to the importance of elementary particles in quantum field theory. While the research progress in the field of particle physics has been rather slow as it requires large-scale high-energy experiments, the studies of quasiparticles in the context of realistic materials have achieved considerable advances in recent years. For instance, the discovery of topological semimetals and superconductors [7–9], which host exotic fermions, has attracted significant attention. In addition to the Weyl, Dirac, and Majorana fermions, condensed matter allows for the realization of quasiparticles that have no counterparts in high-energy physics [10–13], such as the nodal line and nodal net quasiparticles [14–16]. In the nodal net semimetal, the valence and conduction bands touch in momentum space such that the gapless points form a net of connected loops. These materials are predicted to host peculiar drumhead surface states [17,18], which are argued to provide a route to high-temperature superconductivity [19,20]. However, only a few nodal net quasiparticles have been experimentally observed in electronic systems, because they must appear in the vicinity of the Fermi level and they can be destroyed by the effect of spin-orbit coupling [5]. This condition makes the realization of ideal nodal net states challenging in electronic systems.

In recent years, research on topological states has been generalized to bosonic systems, such as photons in photonic crystals [21–23], and classical elastic waves in macroscopic artificial phononic crystals [24–27]. Earlier studies were focused on the behavior of artificial macroscopic mechanical systems in the kHz energy range. With the development of experimental techniques, the investigations of phonon systems are no longer limited to the low-frequency regime. The discovery of Weyl phonons in transition-metal monosilicides [28,29] has provided a route to topological phononics [30–32] at the atomic scale. This has become a motivation to actively explore topological phonon excitations in the THz energy range in natural crystalline materials. In contrast to artificial crystals, topological phonons in realistic materials could play an important role in thermal transports, electron-phonon coupling, or other phonon-related processes [33,34]. Up to now, topological phonons have been reported in many materials [35]. These unconventional phonon states can be classified into nodal point phonons [36–40], nodal ring phonons [41–43], and nodal straight-line phonons [44,45]. Unfortunately, nodal net phonons have not yet been discovered in realistic materials.

In this paper, based on first-principles calculations and effective model analysis, we propose that the nodal net phononic quasiparticle states can be identified in the cuprous oxide (Cu_2O) compound. Similar to the fermionic nodal net, the spectrum of surface phonon excitations in Cu_2O exhibits topological features such as phononic arcs and drumhead structures, which can be identified from the k-resolved spectrum of surface phonons. In contrast to isolated points or loop nodal structures, the nodal net is formed by crossed nodal lines at the boundaries of the Brillouin zone (BZ), which is expected to have a larger contribution to the phonon-related properties. Compared to the fermionic system, the phonon nodal net states in Cu_2O are robust with respect to the time-reversal symmetry breaking due to the lack of spin. The prediction of phononic topological surface states could be verified by existing experimental techniques, such as neutron scattering [46], helium scattering [47], and surface electron

*Corresponding author: a.rudenko@science.ru.nl
†Corresponding author: s.yuan@whu.edu.cn

 ©2021 American Physical Society

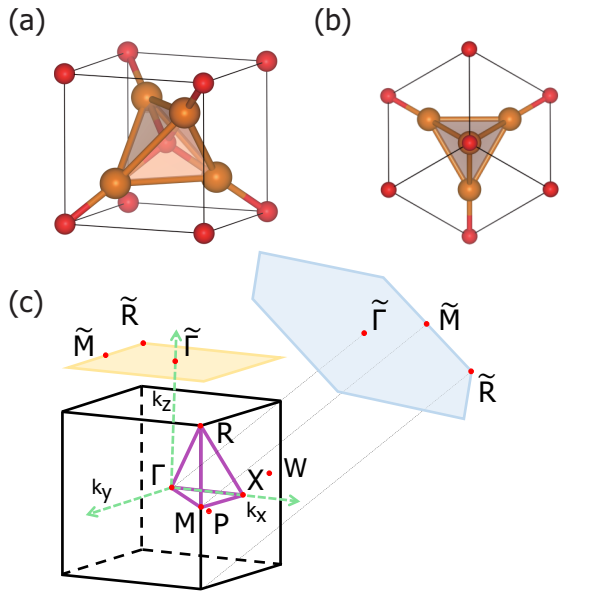

FIG. 1. (a) The crystal structure of Cu_2O and (b) its side view of the (111) surface. (c) The bulk BZ and its projection onto the (001) and (111) surfaces.

energy loss spectroscopy [48]. Therefore, our findings provide a promising avenue for investigations of topologically nontrivial states at the atomic scale, and for further development of phononic devices.

II. CRYSTAL STRUCTURE AND COMPUTATIONAL METHOD

Cu_2O has a cuprite structure with a centrosymmetric space group $Pn\bar{3}m$ (No. 224). The optimized lattice constants are $a = b = c = 4.268$ Å, in accordance with previous experimental results [49]. The primitive cell is composed of six atoms, as is shown in Figs. 1(a) and 1(b). Oxygen atoms are arranged in a body-centered-cubic lattice, and a tetrahedron of Cu atoms surrounds each oxygen atom. The bulk BZ and its projection on the (001) and (111) surfaces are presented in Fig. 1(c). The calculations are performed within the framework of density-functional theory (DFT) [50,51] by using the Vienna ab initio simulation package (VASP) [52,53]. To describe the exchange-correlation effects, the generalized gradient approximation (GGA) within the Perdew-Burke-Ernzerhof (PBE) functional [54] was used. A cutoff energy for the plane-wave expansion was set to 500 eV. The BZ was sampled by a $(13 \times 13 \times 13)$ Monkhorst-Pack mesh [55]. The phonon-related properties are calculated based on the density functional perturbation theory (DFPT) [56] as implemented in the PHONOPY code [57]. For this purpose, a $(3 \times 3 \times 3)$ supercell was constructed to obtain a reliable dynamical matrix. It was checked that nonanalytical corrections do not lead to any significant effect. To reveal the topological features of the phonon nodal net in Cu_2O, we construct a Wannier tight-binding (TB) phonon Hamiltonian from the second rank tensor of force constants as implemented in WANNIERTOOLS [58]. The Berry phase [59,60] of the topological phonon nodal net is calculated using the equation $\gamma_n = \oint_C A_n(\mathbf{k}) \cdot d\mathbf{l}$,

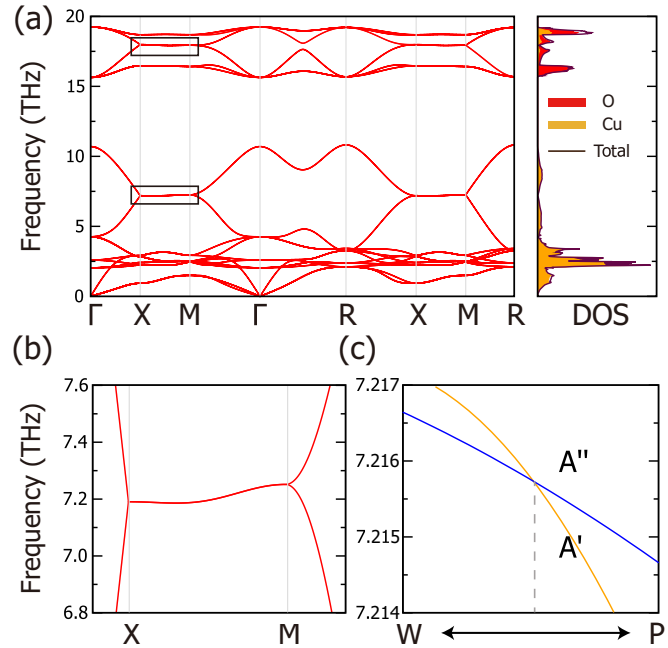

FIG. 2. (a) The calculated phonon spectra and frequency-dependent phonon DOS of Cu_2O. (b) The enlarged phonon spectra marked by a black box in (a). (c) The phonon bands crossing forming a type-II crossing point along the special path W-P [see the BZ in Fig. 1(c) for details]. The two branches belong to the irreducible representations A' and A'' of the point group C_s, respectively.

where $A_n(\mathbf{k}) = -i \sum_n \langle u_n(\mathbf{k}) | \nabla_{\mathbf{k}} | u_n(\mathbf{k}) \rangle$ is the Berry connection, $u_n(\mathbf{k})$ is the Bloch function of the nth band, and C is a closed loop in momentum space.

III. PHONON DISPERSION AND DENSITY OF STATES

In Fig. 2(a), we present the phonon dispersion curves calculated along the high-symmetry lines of the BZ and the corresponding density of states (DOS) of bulk Cu_2O. There are three acoustic branches converging at the Γ point, indicating dynamical stability of the system. The most interesting optical branches appear at frequencies $\omega = 7.2$ and 18 THz along the high-symmetry line X-M, where two branches merge forming almost flat bands [marked by the black box in Fig. 2(a)]. In this region, a vanishing DOS is observed. The DOS at low and high frequencies is dominated by Cu and O atoms, respectively, as can be seen from the partial DOS. As an example, we focus on the flat phonon bands at low phonon frequency (11th and 12th phonon branches). A zoom-in plot of flat phonon branches around 7.2 THz is shown in Fig. 2(b). One can see that the two branches touch and form a nodal straight line lying on the X-M high-symmetry line. There is a tiny energy dispersion along this direction, which makes the phonon nodal line not absolutely flat. Next, to study the phonon band inversion and classify the twofold degeneracy crossing points, we calculate the phonon band structure along a special path. The enlarged view of the phonon spectrum along the W-P direction near the crossing point is shown in Fig. 2(c), where the coordinates of W and P in momentum space are (0.45, −0.50, 0.00) and (0.501, 0.50, 0.00) in units

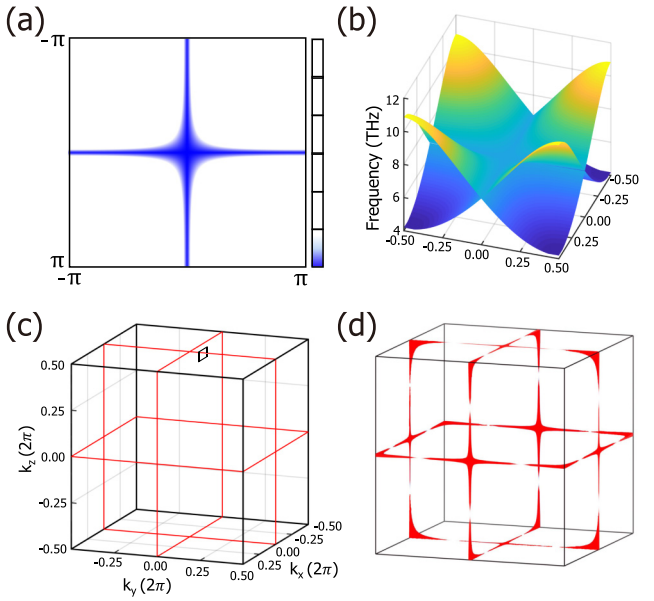

FIG. 3. (a) A map of energy gaps between the two crossing branches around 7.2 THz in the $k_z = \pi/a$ plane. Blue represents the nodal lines (zero gap). (b) A 3D visualization of the 11th and 12th phonon branches in the $k_z = \pi/a$ plane. (c) A 3D map of the gapless points located in the cubic BZ. (d) The isofrequency surface at 7.2 THz.

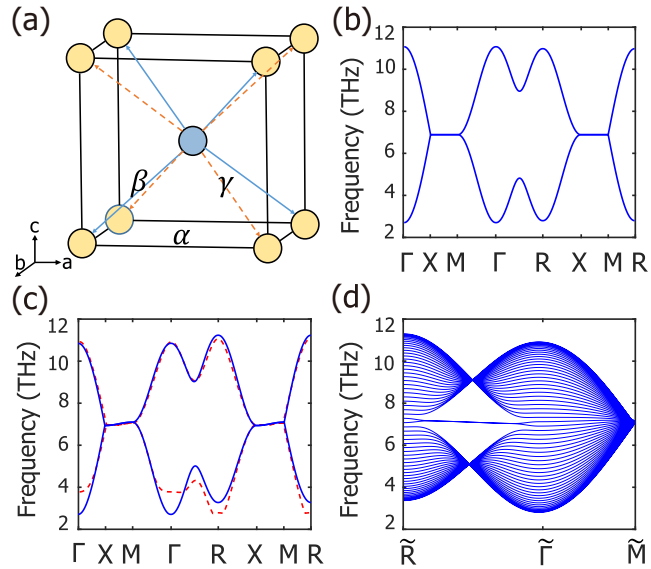

FIG. 4. (a) The effective phonon lattice with two sublattices and hopping vectors indicated by arrows. (b) The TB band structure calculated with $\alpha = 0$, $\beta = -0.01$, and $\gamma = -0.89$ (all in THz). (c) Blue solid lines represent the TB band structure calculated with $\alpha = -0.035$, $\beta = -0.01$, and $\gamma = -0.89$. Red dashed lines represent the results of first-principles calculations. (d) The (001)-projected phononic slab bands calculated from the TB model, where a flat surface band is clearly visible.

$2\pi/a$. The generic **k** points in the $k_z = 0$ plane have the point group symmetry C_s, which includes two different irreducible representations A' and A''. One can see that the two crossing bands form a type-II crossing point.

In the phonon nodal net states, the nodal points are not isolated in momentum space. After carefully scanning the band gap in the $k_z = \pi/a$ plane, we find two phonon nodal straight lines located at the BZ boundary with a peculiar crossing shape, as is shown in Fig. 3(a). Accordingly, the phonon band structure of the crossing branches in the $k_z = \pi/a$ plane is given in Fig. 3(b). Furthermore, these nodal straight lines are perpendicular to each other in different planes, and they form a nodal net in the three-dimensional (3D) BZ as shown in Fig. 3(c). To confirm the topological nature of the phonon nodal net in Cu_2O, we calculate the Berry phase of the A' and A'' bands assuming their half-filling. The integration path of the Berry connection is shown in Fig. 3(c) as a black rectangle. Under the conditions mentioned, the calculated Berry phase is π, which indicates the phonon nodal net is topologically nontrivial. In addition, the isofrequency surface with $\omega = 7.2$ THz is illustrated in Fig. 3(d), which agrees well with the nodal net in the BZ.

IV. LATTICE MODEL OF THE NODAL NET

To better understand the formation of the nodal net located along the X-M high-symmetry line in Cu_2O, we construct a simple TB Hamiltonian of phonons from the real-space interatomic force constants. Specifically, we consider a minimal two-band model with the Hamiltonian defined on a 3D square lattice with two sublattices that are represented by two atoms shown in Fig. 4(a). In **k**-space, the two-band Hamiltonian can be written as

$$H(\boldsymbol{k}) = d_0(\boldsymbol{k}) + \sum_{i=x,y,z} d_i(\boldsymbol{k})\sigma_i, \tag{1}$$

where $d_0(\boldsymbol{k})$ and $d_i(\boldsymbol{k})$ are real functions of momentum $\boldsymbol{k}$, and σ_i are the Pauli matrices. For the case under consideration, the appearance of gapless points requires $d_z(\boldsymbol{k}) = 0$. The functions in [Eq. (1)] are given by

$$d_0(\boldsymbol{k}) = \xi + \alpha(\cos k_x a + \cos k_y a + \cos k_z a), \tag{2}$$

$$\begin{aligned} d_x(\boldsymbol{k}) =& \beta(\cos \boldsymbol{kr}_1 + \cos \boldsymbol{kr}_2 + \cos \boldsymbol{kr}_3 + \cos \boldsymbol{kr}_4) \\ &+ \gamma(\cos \boldsymbol{kr}_5 + \cos \boldsymbol{kr}_6 + \cos \boldsymbol{kr}_7 + \cos \boldsymbol{kr}_8), \end{aligned} \tag{3}$$

$$\begin{aligned} d_y(\boldsymbol{k}) =& -\beta(\sin \boldsymbol{kr}_1 + \sin \boldsymbol{kr}_2 + \sin \boldsymbol{kr}_3 + \sin \boldsymbol{kr}_4) \\ &- \gamma(\sin \boldsymbol{kr}_5 + \sin \boldsymbol{kr}_6 + \sin \boldsymbol{kr}_7 + \sin \boldsymbol{kr}_8), \end{aligned} \tag{4}$$

where ξ is the on-site energy term, α is the hopping parameters between lattice sites of the same sublattice, and β and γ are the hopping parameters between lattice sites of different sublattices. For symmetry reasons, the hopping parameters β and γ are unequal. The hoppings represent the degree of effective interatomic coupling, and they are schematically shown in Fig. 4(a). $\mathbf{r}_i$ ($i = 1$–4) and $\mathbf{r}_j$ ($j = 5$–8) are the hopping vectors shown in Fig. 4(a) by blue solid lines and yellow dashed lines, respectively. The corresponding energy dispersion can be calculated as

$$E_{\pm}(\boldsymbol{k}) = d_0(\boldsymbol{k}) \pm \sqrt{d_x^2(\boldsymbol{k}) + d_y^2(\boldsymbol{k})}, \tag{5}$$

from which the band crossing appears when $d_x(\boldsymbol{k}) = d_y(\boldsymbol{k}) = 0$. The band crossing along the X-M high-symmetry line

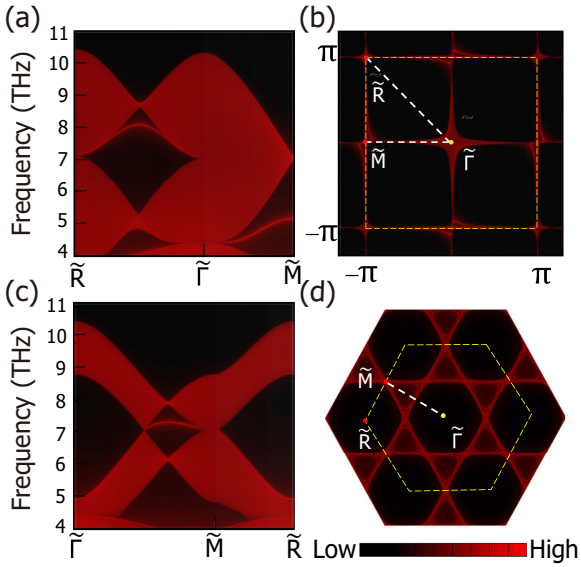

FIG. 5. Phonon surface LDOS of Cu_2O and the corresponding phononic arcs at 7.2 THz. (a) The phonon LDOS projected on the semi-infinite (001) surface along $\tilde{R}$-$\tilde{\Gamma}$-$\tilde{M}$. (b) The phonon surface phononic arc for the (001) surface. (c) The LDOS projected on the semi-infinite (111) surface along $\tilde{\Gamma}$-$\tilde{M}$-$\tilde{R}$. (d) The phonon surface phononic arc for the (111) surface. The region inside the yellow dashed line denotes the surface BZ.

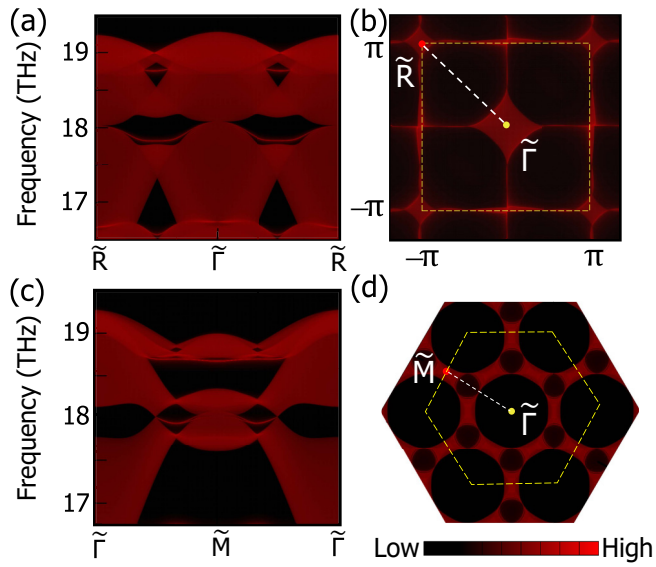

FIG. 6. Phonon surface states and corresponding arcs of Cu_2O at 18 THz. (a) The phonon LDOS projected on the semi-infinite (001) surface along $\tilde{R}$-$\tilde{\Gamma}$-$\tilde{R}$. (b) The phonon surface phononic arc for the (001) surface. (c) The LDOS projected on the semi-infinite (111) surface along $\tilde{\Gamma}$-$\tilde{M}$-$\tilde{\Gamma}$. (d) The phonon surface phononic arc for the (111) surface.

originates from the hoppings between different sublattices. When $\alpha = 0$ and $\beta \neq \gamma$, the nodal net appears along the X-M high-symmetry line at the BZ boundary, and the corresponding band structure is strictly flat, as is shown in Fig. 4(b). To more accurately reproduce the results of first-principles calculations, we fit parameters of the TB model as $\xi = 7.2$, $\alpha = -0.035$, $\beta = -0.01$, and $\gamma = -0.89$ (all in THz). The corresponding TB band structures are shown in Fig. 4(c) in comparison with the results of first-principles calculations. The hopping amplitudes between different sublattices are significantly larger than those within the same sublattice. Moreover, the intrasublattice hopping term α breaks chiral symmetry and causes slight dispersion of the band structure along the X-M high-symmetry line. On the other hand, the chiral symmetry can be restored by setting α to zero [see Fig. 4(b)].

Due to the bulk-boundary correspondence, the nontrivial nodal net structure leads to the formation of a drumlike surface state [18]. To find out the role of surface states in Cu_2O, we use a similar method to that in Ref. [61] to construct a 20-unit-cell-thick slab with O atom termination stacked along the [001] direction. The phononic bands calculated for the slab are shown in Fig. 4(d), where an isolated surface band is located in between the nodal net states connecting the gapless points [62]. The chiral symmetry is broken by the intrasublattice hopping term α, thus the surface band is not perfectly flat having a tiny bandwidth. This indicates that the surface states would not be dispersionless in a real material system.

Next, we make a detailed analysis of symmetry to interpret the formation of a nodal net shown in Fig. 3(c). The nonmagnetic space group $Pn\bar{3}m$ contains the glide planes $\tilde{M}_x = \{M_x|0, 1/2, 1/2\}$, $\tilde{M}_y = \{M_y|1/2, 0, 1/2\}$, and $\tilde{M}_z = \{M_z|1/2, 1/2, 0\}$, and they are the products of symmetry operators and fractional translational vectors in the unit of the lattice constant a. On the other hand, the time-reversal ($\mathcal{T}$) symmetry of the phonon system is always conserved. If we consider the transformations of a $\boldsymbol{k}$ point under the operations of $\tilde{M}_x$ and $\mathcal{T}$, we have

$$(k_x, k_y, k_z) \xrightarrow{\tilde{M}_x} (-k_x, k_y, k_z) \xrightarrow{\mathcal{T}} (k_x, -k_y, -k_z). \quad (6)$$

Under this combined transformation, the line $\boldsymbol{k} = (k_x, 0, \pm\pi/a)$ is invariant, indicating that the product operation $\tilde{M}_x\mathcal{T}$ commutes with Hamiltonian $H(\boldsymbol{k})$ if $\boldsymbol{k}$ is along this invariant line. Due to the spinless nature of the phonon, we can get $\mathcal{T}^2 = 1$ and $\tilde{M}_x^2\mathcal{T}^2 = e^{ik_ya}e^{ik_za}$. Thus, $\tilde{M}_x^2\mathcal{T}^2 = -1$ satisfies the Kramers-like degeneracy for $\boldsymbol{k}$ points along the high-symmetry line $\boldsymbol{k} = (k_x, 0, \pm\pi/a)$, resulting in the appearance of this nodal line. Similarly, the appearance of the other nodal lines shown in Fig. 3(c) can also be explained by the combined transformations of $\mathcal{T}$ and the corresponding glide planes.

V. SURFACE PHONON STATES AND THEIR TOPOLOGICAL FEATURES

Topological surface states can serve as evidence of the nontrivial nodal structure of a material. To better understand the behavior of surface states in Cu_2O, we calculate the local density of surface states (LDOS), and we restore the isofrequency contours. To this end, we use the iterative Green's function method [63] with a full phonon TB Hamiltonian as implemented in the WANNIERTOOLS package [58]. The results are shown in Figs. 5 and 6, where the intensity of the LDOS is represented by a color bar.

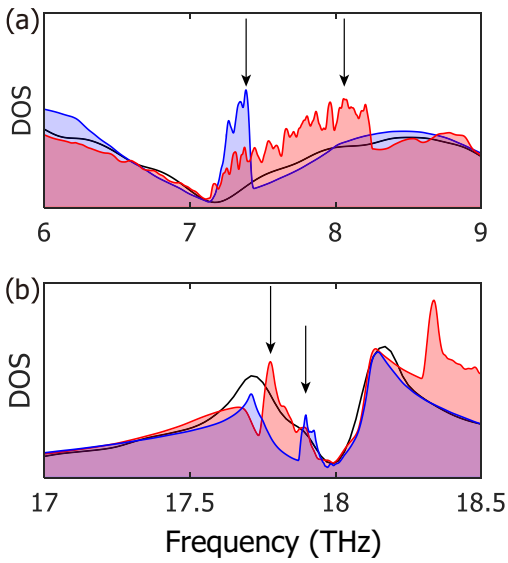

FIG. 7. Surface phonon DOS and bulk DOS in the low-frequency (a) and high-frequency range (b) of nodal net states. The black line corresponds to bulk DOS. Red and blue lines represent the (001) and (111) surface-projected DOS, respectively.

We first consider the (001) surface with O atom termination in the low-frequency range. The LDOS calculated along the surface momentum lines $\tilde{R}$-$\tilde{\Gamma}$-$\tilde{M}$ is shown in Fig. 5(a). As expected for nodal-line materials [41–43], the drumhead surface states connecting the $\tilde{R}$ and $\tilde{\Gamma}$ points appear around 7.2 THz. Its corresponding isofrequency contour is shown in Fig. 5(b). In addition, the surface phonon LDOS as well as the surface phononic arcs for the (111) surface calculated along the surface path $\tilde{\Gamma}$-$\tilde{M}$-$\tilde{R}$ are shown in Figs. 5(c) and 5(d). One can see that the surface states along $\tilde{\Gamma}$-$\tilde{M}$ are essentially flat and well isolated from the bulk states. The BZ of the (111) surface is a hexagon, and the surface phononic arcs form six trianglelike curves in the surface BZ. Unlike the previously proposed phononic material whose surface states are buried in the bulk states and have a considerable energy dispersion, the surface states in Cu_2O are separated from the bulk states and essentially dispersionless. This observation may be beneficial for further studies of phonon-related properties of topological surfaces [64] and for the design of potential phonon devices [31].

The calculated phonon surface states and arcs of Cu_2O in the high-frequency range are shown in Fig. 6. In this situation, the surface states and arcs are overall similar to the 7.2 THz case. In contrast to the low-frequency range, the band structure at high frequencies along the Γ-R high-symmetry line exhibits a small gap [see Fig. 2(a)], and the dispersion along the X-M direction is more pronounced than at 7.2 THz. This results in a difference between the surface states in the low- and high-frequency range. In Figs. 6(a) and 6(b), we demonstrate the surface phonon LDOS and corresponding isofrequency contour for the (001) surface. One can clearly see the uncovered surface states and phononic arcs. Meanwhile, the surface states and phononic arcs for the (111) surface are shown in Figs. 6(c) and 6(d) as well. It should be noted that not many topological materials guarantee that their surface states are clearly observed, because the bulk states projected onto the material surface cover the surface states [41,44]. Here, we propose that the topological surface states in Cu_2O with O atom termination are clean, allowing for their experimental detection, e.g., by means of helium atom energy loss spectroscopy or inelastic x-ray scattering [29,47].

Phonon-related observable properties are often averaged over the k-space, i.e., they depend primarily on phonon DOS. We have calculated the (001) and (111) surface phonon DOS of Cu_2O, which is shown in Figs. 7(a) and 7(b). Here, we only consider the surface DOS at frequencies around the topological nodal nets. For comparison, the bulk DOS is shown by a black line, which exhibits a minimum at the frequency of the nodal net. In comparison to bulk DOS, the surface DOS displays prominent peaks at 7.2 and 17.8 THz, which are marked by black arrows in Fig. 7. As can be seen from Figs. 5 and 6, the surface peaks originate from the contribution of nontrivial drumhead surface states. Furthermore, the degree of localization of the peaks is closely related to the dispersion of the surface states.

VI. CONCLUSION

In summary, by using first-principles calculations and effective model analysis, we demonstrate that the nodal net phonons are present in Cu_2O. The nodal net is represented by straight lines constrained in the high-symmetry line X-M at the BZ boundary. The absence of spin in phononic systems ensures that the nodal net phonons in Cu_2O are robust with respect to the time-reversal symmetry breaking. The nontrivial phonon surface states are clearly visible in k-resolved energy spectra projected on the (001) and (111) surfaces with O atom termination. The surface states give rise to distinct resonances in DOS, which may contribute to phonon transport properties and play a role in interfacial superconductivity. Our findings demonstrate that Cu_2O is a promising candidate for studying topological properties involving vibrational degrees of freedom.

ACKNOWLEDGMENTS

This work is supported by the National Key R&D Program of China (Grant No. 2018YFA0305800) and Natural Science Foundation of Hubei Province, China (2020CFA041). Numerical calculations presented in this paper have been performed on the supercomputing system in the Supercomputing Center of Wuhan University.

Z.W.W. and W.Q.Z. contributed equally to this work.

[1] Z. K. Liu, B. Zhou, Y. Zhang, Z. J. Wang, H. M. Weng, D. Prabhakaran, S.-K. Mo, Z. X. Shen, Z. Fang, X. Dai, Z. Hussain, and Y. L. Chen, Discovery of a three-dimensional topological Dirac semimetal, Na_3Bi, Science **343**, 864 (2014).

[2] Z. Wang, Y. Sun, X.-Q. Chen, C. Franchini, G. Xu, H. Weng, X. Dai, and Z. Fang, Dirac semimetal and topological phase transitions in A_3Bi (A = Na , K, Rb), Phys. Rev. B **85**, 195320 (2012).

[3] A. A. Burkov, M. D. Hook, and L. Balents, Topological nodal semimetals, Phys. Rev. B **84**, 235126 (2011).

[4] N. P. Armitage, E. J. Mele, and A. Vishwanath, Weyl and Dirac semimetals in three-dimensional solids, Rev. Mod. Phys. **90**, 015001 (2018).

[5] H. Weng, C. Fang, Z. Fang, B. A. Bernevig, and X. Dai, Weyl Semimetal Phase in Noncentrosymmetric Transition-Metal Monophosphides, Phys. Rev. X **5**, 011029 (2015).

[6] Z. Wang, M. G. Vergniory, S. Kushwaha, M. Hirschberger, E. V. Chulkov, A. Ernst, N. P. Ong, R. J. Cava, and B. A. Bernevig, Time-Reversal-Breaking Weyl Fermions in Magnetic Heusler Alloys, Phys. Rev. Lett. **117**, 236401 (2016).

[7] L. Fu and C. L. Kane, Superconducting Proximity Effect and Majorana Fermions at the Surface of a Topological Insulator, Phys. Rev. Lett. **100**, 096407 (2008).

[8] X.-L. Qi and S.-C. Zhang, Topological insulators and superconductors, Rev. Mod. Phys. **83**, 1057 (2011).

[9] S. Nadj-Perge, I. K. Drozdov, J. Li, H. Chen, S. Jeon, J. Seo, A. H. MacDonald, B. A. Bernevig, and A. Yazdani, Observation of Majorana fermions in ferromagnetic atomic chains on a superconductor, Science **346**, 602 (2014).

[10] B. Q. Lv, Z.-L. Feng, Q.-N. Xu, X. Gao, J.-Z. Ma, L.-Y. Kong, P. Richard, Y.-B. Huang, V. N. Strocov, C. Fang, H.-M. Weng, Y.-G. Shi, T. Qian, and H. Ding, Observation of three-component fermions in the topological semimetal molybdenum phosphide, Nature (London) **546**, 627 (2017).

[11] B. Bradlyn, J. Cano, Z. Wang, M. G. Vergniory, C. Felser, R. J. Cava, and B. A. Bernevig, Beyond Dirac and Weyl fermions: Unconventional quasiparticles in conventional crystals, Science **353**, aaf5037 (2016).

[12] Z. Zhu, G. W. Winkler, Q. Wu, J. Li, and A. A. Soluyanov, Triple Point Topological Metals, Phys. Rev. X **6**, 031003 (2016).

[13] A. A. Soluyanov, D. Gresch, Z. Wang, Q. Wu, M. Troyer, X. Dai, and B. A. Bernevig, Type-II Weyl semimetals, Nature (London) **527**, 495 (2015).

[14] T. Bzdušek, Q. Wu, A. Rüegg, M. Sigrist, and A. A. Soluyanov, Nodal-chain metals, Nature (London) **538**, 75 (2016).

[15] R. Yu, H. Weng, Z. Fang, X. Dai, and X. Hu, Topological Node-Line Semimetal and Dirac Semimetal State in Antiperovskite Cu_3PdN, Phys. Rev. Lett. **115**, 036807 (2015).

[16] X. Feng, C. Yue, Z. Song, Q. Wu, and B. Wen, Topological Dirac nodal-net fermions in AlB_2-type TiB_2 and ZrB_2, Phys. Rev. Mater. **2**, 014202 (2018).

[17] H. Weng, Y. Liang, Q. Xu, R. Yu, Z. Fang, X. Dai, and Y. Kawazoe, Topological node-line semimetal in three-dimensional graphene networks, Phys. Rev. B **92**, 045108 (2015).

[18] G. Bian, T.-R. Chang, H. Zheng, S. Velury, S.-Y. Xu, T. Neupert, C.-K. Chiu, D. S. Sanchez, I. Belopolski, N. Alidoust, P.-J. Chen, G. Chang, A. Bansil, H.-T. Jeng, H. Lin, and M. Z. Hasan, Drumhead surface states and topological nodal-line fermions in $TlTaSe_2$, Phys. Rev. B **93**, 121113(R) (2016).

[19] T. T. Heikkilä, N. B. Kopnin, and G. E. Volovik, Flat bands in topological media, JETP Lett. **94**, 233 (2011).

[20] T. T. Heikkilä and G. E. Volovik, *Basic Physics of Functionalized Graphite* (Springer, New York, 2016).

[21] F. D. M. Haldane and S. Raghu, Possible Realization of Directional Optical Waveguides in Photonic Crystals with Broken Time-Reversal Symmetry, Phys. Rev. Lett. **100**, 013904 (2008).

[22] L. Lu, L. Fu, J. D. Joannopoulos, and M. Soljačić, Weyl points and line nodes in gyroid photonic crystals, Nat. Photon. **7**, 294 (2013).

[23] Z. Wang, Y. D. Chong, J. D. Joannopoulos, and M. Soljačić, Reflection-Free One-Way Edge Modes in a Gyromagnetic Photonic Crystal, Phys. Rev. Lett. **100**, 013905 (2008).

[24] S. H. Mousavi, A. B. Khanikaev, and Z. Wang, Topologically protected elastic waves in phononic metamaterials, Nat. Commun. **6**, 8682 (2015).

[25] R. Süsstrunk and S. D. Huber, Observation of phononic helical edge states in a mechanical topological insulator, Science **349**, 47 (2015).

[26] F. Li, X. Huang, J. Lu, J. Ma, and Z. Liu, Weyl points and Fermi arcs in a chiral phononic crystal, Nat. Phys. **14**, 30 (2018).

[27] B. Xie, H. Liu, H. Cheng, Z. Liu, S. Chen, and J. Tian, Experimental Realization of Type-II Weyl Points and Fermi Arcs in Phononic Crystal, Phys. Rev. Lett. **122**, 104302 (2019).

[28] T. Zhang, Z. Song, A. Alexandradinata, H. Weng, C. Fang, L. Lu, and Z. Fang, Double-Weyl Phonons in Transition-Metal Monosilicides, Phys. Rev. Lett. **120**, 016401 (2018).

[29] H. Miao, T. T. Zhang, L. Wang, D. Meyers, A. H. Said, Y. L. Wang, Y. G. Shi, H. M. Weng, Z. Fang, and M. P. M. Dean, Observation of Double Weyl Phonons in Parity-Breaking FeSi, Phys. Rev. Lett. **121**, 035302 (2018).

[30] W.-C. Ji and J.-R. Shi, Topological phonon modes in a two-dimensional Wigner crystal, Chin. Phys. Lett. **34**, 036301 (2017).

[31] Y. Liu, Y. Xu, S.-C. Zhang, and W. Duan, Model for topological phononics and phonon diode, Phys. Rev. B **96**, 064106 (2017).

[32] L. Zhang, J. Ren, J.-S. Wang, and B. Li, Topological nature of the phonon Hall effect, Phys. Rev. Lett. **105**, 225901 (2010).

[33] A. Chaudhuri, A. Kundu, D. Roy, A. Dhar, J. L. Lebowitz, and H. Spohn, Heat transport and phonon localization in mass-disordered harmonic crystals, Phys. Rev. B **81**, 064301 (2010).

[34] S. Zhang, J. Guan, X. Jia, B. Liu, W. Wang, F. Li, L. Wang, X. Ma, Q. Xue, J. Zhang, E. W. Plummer, X. Zhu, and J. Guo, Role of $SrTiO_3$ phonon penetrating into thin FeSe films in the enhancement of superconductivity, Phys. Rev. B **94**, 081116(R) (2016).

[35] J. Li, J. Liu, S. A. Baronett, M. Liu, L. Wang, R. Li, Y. Chen, D. Li, Q. Zhu, and X.-Q. Chen, Computation and data driven discovery of topological phononic materials, Nat. Commun. **12**, 1204 (2021).

[36] J. Li, Q. Xie, S. Ullah, R. Li, H. Ma, D. Li, Y. Li, and X.-Q. Chen, Coexistent three-component and two-component Weyl phonons in TiS, ZrSe, and HfTe, Phys. Rev. B **97**, 054305 (2018).

[37] Y. Jin, R. Wang, and H. Xu, Recipe for Dirac phonon states with a quantized valley Berry phase in two-dimensional hexagonal lattices, Nano Lett. **18**, 7755 (2018).

[38] J. Liu, W. Hou, E. Wang, S. Zhang, J.-T. Sun, and S. Meng, Ideal type-II Weyl phonons in wurtzite CuI, Phys. Rev. B **100**, 081204(R) (2019).

[39] B. W. Xia, R. Wang, Z. J. Chen, Y. J. Zhao, and H. Xu, Symmetry-Protected Ideal Type-II Weyl Phonons in CdTe, Phys. Rev. Lett. **123**, 065501 (2019).

[40] R. Wang, B. W. Xia, Z. J. Chen, B. B. Zheng, Y. J. Zhao, and H. Xu, Symmetry-Protected Topological Triangular Weyl Complex, Phys. Rev. Lett. **124**, 105303 (2020).

[41] Y. J. Jin, Z. J. Chen, B. W. Xia, Y. J. Zhao, R. Wang, and H. Xu, Ideal intersecting nodal-ring phonons in bcc C_8, Phys. Rev. B **98**, 220103(R) (2018).

[42] T. Zhang, L. Lu, S. Murakami, Z. Fang, H. Weng, and C. Fang, Diagnosis scheme for topological degeneracies crossing high-symmetry lines, Phys. Rev. Research **2**, 022066(R) (2020).

[43] J. Li, L. Wang, J. Liu, R. Li, Z. Zhang, and X.-Q. Chen, Topological phonons in graphene, Phys. Rev. B **101**, 081403(R) (2020).

[44] J. Li, Q. Xie, J. Liu, R. Li, M. Liu, L. Wang, D. Li, Y. Li, and X.-Q. Chen, Phononic Weyl nodal straight lines in MgB_2, Phys. Rev. B **101**, 024301 (2020).

[45] Q.-B. Liu, H.-H. Fu, G. Xu, R. Yu, and R. Wu, Categories of phononic topological Weyl open nodal lines and a potential material candidate: $Rb_2Sn_2O_3$, J. Phys. Chem. Lett. **10**, 4045 (2019).

[46] O. Delaire, I. I. Al-Qasir, A. F. May, C. W. Li, B. C. Sales, J. L. Niedziela, J. Ma, M. Matsuda, D. L. Abernathy, and T. Berlijn, Heavy-impurity resonance, hybridization, and phonon spectral functions in $Fe_{1-x}M_xSi$ (M = Ir,Os), Phys. Rev. B **91**, 094307 (2015).

[47] U. Harten and J. P. Toennies, Surface phonons on GaAs(110) measured by inelastic helium atom scattering, Europhys. Lett. **4**, 833 (1987).

[48] X. Zhu, Y. Cao, S. Zhang, X. Jia, Q. Guo, F. Yang, L. Zhu, J. Zhang, E. W. Plummer, and J. Guo, High resolution electron energy loss spectroscopy with two-dimensional energy and momentum mapping, Rev. Sci. Instrum. **86**, 083902 (2015).

[49] B. Li, X. Wang, D. Xia, Q. Chu, X. Liu, F. Lu, and X. Zhao, One-step Green synthesis of cuprous oxide crystals with truncated octahedra shapes via a high pressure flux approach, J. Solid State Chem. **184**, 2097 (2011).

[50] W. Kohn and L. J. Sham, Self-consistent equations including exchange and correlation effects, Phys. Rev. **140**, A1133 (1965).

[51] P. Hohenberg and W. Kohn, Inhomogeneous electron gas, Phys. Rev. **136**, B864 (1964).

[52] G. Kresse and J. Furthmüller, Efficiency of ab-initio total energy calculations for metals and semiconductors using a plane-wave basis set, Comput. Mater. Sci. **6**, 15 (1996).

[53] G. Kresse and J. Furthmüller, Efficient iterative schemes for *ab initio* total-energy calculations using a plane-wave basis set, Phys. Rev. B **54**, 11169 (1996).

[54] J. P. Perdew, K. Burke, and M. Ernzerhof, Generalized Gradient Approximation Made Simple, Phys. Rev. Lett. **77**, 3865 (1996).

[55] H. J. Monkhorst and J. D. Pack, Special points for Brillouin-zone integrations, Phys. Rev. B **13**, 5188 (1976).

[56] S. Baroni, S. de Gironcoli, A. Dal Corso, and P. Giannozzi, Phonons and related crystal properties from density-functional perturbation theory, Rev. Mod. Phys. **73**, 515 (2001).

[57] A. Togo and I. Tanaka, First principles phonon calculations in materials science, Scr. Mater. **108**, 1 (2015).

[58] Q. Wu, S. Zhang, H.-F. Song, M. Troyer, and A. A. Soluyanov, WannierTools: An open-source software package for novel topological materials, Comput. Phys. Commun. **224**, 405 (2018).

[59] C. Fang, Y. Chen, H.-Y. Kee, and L. Fu, Topological nodal line semimetals with and without spin-orbital coupling, Phys. Rev. B **92**, 081201(R) (2015).

[60] R. Yu, X. L. Qi, A. Bernevig, Z. Fang, and X. Dai, Equivalent expression of $\mathbb{Z}_2$ topological invariant for band insulators using the non-Abelian Berry connection, Phys. Rev. B **84**, 075119 (2011).

[61] Y. Du, F. Tang, D. Wang, L. Sheng, E.-j. Kan, C.-G. Duan, S. Y. Savrasov, and X. Wan, CaTe: a new topological node-line and Dirac semimetal, npj Quantum Mater. **2**, 3 (2017).

[62] B. A. Bernevig and T. L. Hughes, *Topological Insulators and Topological Superconductors* (Princeton University Press, Princeton, NJ, 2013).

[63] M. P. L. Sancho, J. M. L. Sancho, and J. Rubio, Quick iterative scheme for the calculation of transfer matrices: Application to Mo (100), J. Phys. F **14**, 1205 (1984).

[64] R. Li, J. Li, L. Wang, J. Liu, H. Ma, H.-F. Song, D. Li, Y. Li, and X.-Q. Chen, Underlying Topological Dirac Nodal Line Mechanism of the Anomalously Large Electron-Phonon Coupling Strength on a Be (0001) Surface, Phys. Rev. Lett. **123**, 136802 (2019).